4

Experimental method

4.1 Beamline characterization and optics

The experiments reported in this thesis were performed at the National Synchrotron Light Source (NSLS) at Brookhaven National Laboratory and at the Cornell High Energy Synchrotron Source (CHESS) during a test of the Advanced Photon Source (APS) undulator. Fig 2.4 shows a typical experimental setup.

The X25 beamline has been described in detail elsewhere [80, 81]. In short, the X-rays are generated by a 27 pole hybrid wiggler with a peak field of 1 T, installed on a straight section of the 2.5 GeV NSLS storage ring. This wiggler source is characterized by a deflection parameter $K = 12.3$, a characteristic opening angle $K/\gamma = 2.5$ mrad, and a critical energy of 4.6 keV. With a ring current of 230 mA, this source generates a total power of 1.8 kW. For our experiment, the gap was set at 24 mm.

The characteristic distances at X25 are shown in Table 2.1. To control the coherence lengths, two sets of upstream slits at 10.5 m from the source could be closed to reduce the effective source size. A double Si(111) monochromator was used to select 6.9 keV X-rays. The monochromator was slightly detuned from the Bragg condition to filter the third harmonic out. Two types of incident intensity monitors were used: an air filled ion chamber and a film of polyimide oriented at 45 ° from the incident beam, which scatters X-rays into a scintillation counter. Since the absorption length of 6.9 KeV X-rays in air is of the order of 0.5 m, vacuum flight paths were used to reduce X-ray absorption.

To ensure that the beam incident on the sample remained approximately defined by the pinhole diameter, we placed the sample in the near field diffraction region of the pinhole [82] such that the pinhole to center of rotation distance

$$R_c < D^2/\lambda, \tag{4.1}$$

where D is the pinhole diameter. For the smallest pinhole used, $D = 3.5\ \mu$m and $\lambda = 1.797$ Å, which gives the condition $R_c < 6.8$ cm. The input pinholes were placed at $R_c = 6.75$ cm, which is well within the near field of the pinhole diffraction pattern for the measurements done with the 7.5, 15, 33 μm pinholes, but is on the edge of this region for the 3.5 μm pinhole. This is the closest distance achievable for our X-ray oven.

To determine and control the transverse coherence lengths, one must know the source size accurately. At X-25 the source size was measured by scanning the upstream x-y slits (see Fig. 2.4) to cut the beam totally while recording the intensity at the sample position behind a 3.5 μm pinhole. The beam profile is obtained by taking a derivative of the signal. The beam profile is then least-squared fitted using a Gaussian at the slit position, 10.5 m from the source. The horizontal and vertical fitted widths[1] are respectively $\sigma_x = 0.386$ mm, $\sigma_y = 0.0179$ mm at 6.9 keV. Since the point of observation is 27.8 m from the source, the source size near the wiggler is $\sigma_x = 0.62$ and $\sigma_y = 0.0288$ mm.

The CHESS synchrotron ring was operated at 5.437 GeV, with a maximum current of 100 mA [83]. The undulator was a prototype of the APS undulators. This undulator is made of 123 magnetic poles with 3.3 cm periods, and its fundamental energy can be tuned from 4.3 to 7.9 keV [83]. The undulator gap was set at 2.3 cm in order to tune to the 7 keV fundamental. The double Si (111) monochromator was set to diffract 7.0 keV X-rays. Since the source horizontal size $d_{sx} = 2.55$ mm is approximately twice larger at CHESS compared with X25, a 0.4 mm horizontal slit was placed 17.8 m from the source to limit the horizontal source size.

[1] The Gaussian fit used was $I(x) = I_0 exp(-.5(x - x_0)^2/\sigma_x^2))$, where x_0 is the peak center, σ_x the width, and I_0 the peak intensity.

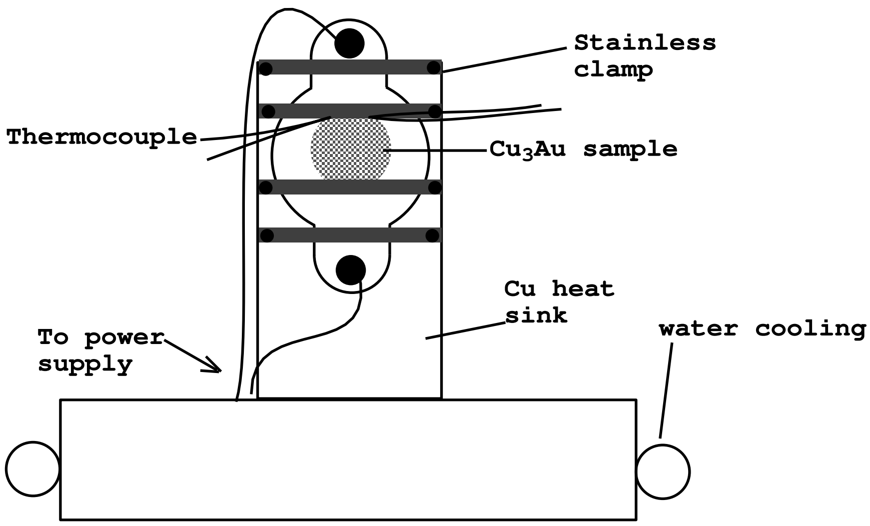

Figure 4.1: The X-ray oven.

4.2 Sample preparation and sample furnace

The sample preparation at the Oak Ridge National Laboratories has been previously described in detail [31, 32]. The sample surface normal is oriented along the [100]. A vacuum sample chamber was designed to heat the sample to elevated temperatures and to prevent its oxidation. The sample furnace essential element is a 6Ω pyrolytic Boron Nitride coated pyrolytic graphite heater[1] mounted on a water cooled Cu heat sink which gives sufficient cooling power to quench the sample rapidly. The sample was mounted on the heater using stainless steel clamps screwed on the Cu block. With this design, quench rates of a few Kelvin per second could be easily attained. The maximum temperature reached by this oven could be adjusted by thermally insulating the back of the heater and the Cu heat sink with varying thicknesses of mica. The mica limits the heat flow to the heat sink and increases the temperature difference between the heater and Cu block. A commercial proportional temperature controller (Omega CN8031) was used to maintain the set point temperature constant to within 0.1°C using a standard proportional, integral and differential control loop. Two type-K thermocouples recorded the sample temperature and the control temperature. A

[1]The heater is a 2 cm diameter Boralectric^{TM} PBN/PG resistance heating element, purchased from Union Carbide Coatings Service Corporation, P.O Box 94924, Cleveland, OH, USA, 44101-4924.

standard cold junction compensator (Omega-CJ-K) was used to set the ice point reference of the sample thermocouple. The thermocouples were held in contact with the sample by the clamps. The X-rays could penetrate the sample chamber through a 180 degree Be window, 0.015 inch thick[1]. A DC power supply, controlled by the temperature controller through an operational amplifier input, generated a current from zero to six A which is required because of the small heater resistance.

4.3 *Scattering geometry*

Fig. 4.2 shows the scattering geometry for this experiment. The CCD or the scintillator is mounted on a standard 4 circle Huber diffractometer, computer controlled to scan the three sample angles θ, ϕ, and χ, and the central detector angle 2θ, which defines, with the incoming beam direction, the scattering plane. The scattering plane is vertical. The sample is mounted on the ϕ circle of the diffractometer, and the four angles are set for the (100) reflection.

Because the CCD is able to measure outgoing wavevectors in two directions, we use the central pixel to define a scattering plane. Thus, $2\theta_\perp$ is the angle perpendicular to the plane, and $2\theta_{||}$ is in the plane. Here $2\theta_{||}$ is like the usual detector angle. In Fig. 4.2, θ_i is the angle of incidence of the X-ray beam with respect to the surface. Following Ref [16], one can show that the components of the scattering wavevector $\vec{q} = \vec{k}_f - \vec{k}_i$ in the sample coordinates are

$$\begin{aligned} q_x &= k \sin 2\theta_\perp \approx kx'/R_d, \\ q_y &= k(\cos 2\Theta_\perp \cos(2\theta_{||} - \theta_i) - \cos\theta_i) \approx k(\cos(2\theta_B + y'/R_d - \theta_i) - \cos\theta_i), \quad (4.2) \\ q_z &= k(\cos 2\Theta_\perp \sin(2\theta_{||} - \theta_i) + \sin\theta_i) \approx k(\sin(2\theta_B + y'/R_d - \theta_i) + \sin\theta_i), \end{aligned}$$

where $k = 2\pi/\lambda$. The sample x-axis is oriented along the theta axis of rotation, while the z-axis is oriented along the surface normal. The x' and y' axes are the pixel coordinates in the detector plane, centered on the Bragg angle $2\theta_B$.

[1]This Be thickness absorbs 11 % of the 7 KeV X-rays.

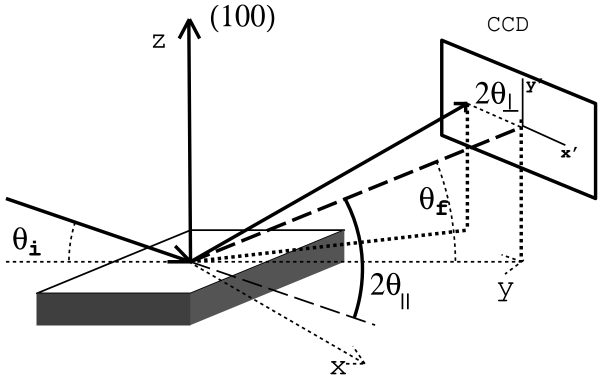

Figure 4.2: The scattering geometry. The Cu_3Au (100) is along the z-axis. The angle of incidence θ_i and the scattered angle θ_f are measured with respect to the sample surface. The angle $2\theta_{\|}$ is the usual detector angle.

4.4 Data treatment

The scattered X-rays were measured with the CCD described in Chapter 3. The data acquisition was stopped regularly to record a dark pattern without X-rays. This dark pattern slowly drifted in time over several hours and was monitored regularly. For the data acquired at X-25, this drift was correlated with an NSLS lab cooling water temperature drift[1], which affected the CCD chip temperature because this water cooled the CCD Peltier stage[2]. This drift was of the order of one or two X-ray photons, but could easily be corrected by subtracting the most recent dark pattern. Furthermore, the four corners of the CCD were masked by lead to absorb all incident X-rays, so these areas were used to keep track of the drift in the dark pattern.

At X25, the detector signal was calibrated against a scintillation detector with a quantum efficiency of nearly 100%, in order to correct the detector non-linearity. After a dark signal subtraction, the detected signal was rescaled with this calibration using Eq. 3.20.

During the CHESS experiment, one of the CCD amplifiers was different than during the X25 experiment. For a given incident count rate and exposure time, if one assumes that the raw data measured at CHESS only differs from the X25 calibration

[1] For example, it has been shown that the temperature drift in the cooling water at NSLS affects the bending magnet alignment causing orbit motion[84].

[2] This problem has since been fixed by cooling the Peltier stage with a recirculating temperature-controlled water bath.

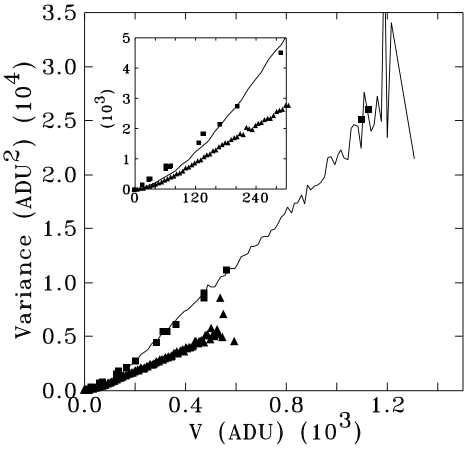

Figure 4.3: The measured CCD signal variance versus the mean. The calibration at X25 and CHESS are respectively shown with squares and triangles. The solid line represents the CHESS data rescaled by a factor 2.2 for the mean and $(2.2)^2$ for the variance.

by a multiplicative constant, one can use Eq. 3.20 to rescale the CHESS data into photons. It is shown in Fig. 4.3 that this constant is $a = 2.2$ so that the signal at X25, V_X, is equal to aV_C, where V_C is the signal at CHESS, and the variance at X25, S_X^2 is equal to $a^2S_C^2$. This rescaling is excellent for count rates above 160 ADU. As shown in the inset, some difference is seen for small count rates.

To compensate for the slow decay of the incident synchrotron radiation intensity, the signal was scaled to the incident beam intensity measured by an air filled ion chamber beam monitor[1]. After linearization and normalization to the incident intensity, the floating point signal was multiplied by a factor 100 and then saved into a two byte short integer array for further analysis.

4.5 *Pinhole construction*

The pinholes were made by laser drilling through 50 μm thick Pt foils[2]. The pinholes used are really *pinhole tunnels* because their diameters are smaller than their 50 μm thickness. The foils were glued on a 1.0 mm thick Ta mount, pierced with a hole of diameter $D_m = 0.5$ mm. The ratio of transmitted intensity through a pinhole of diam-

[1] This detector measures the ionized current between two high voltage electrodes due to the photoionization of gas molecules. This signal is proportional to the incident intensity when there is no dielectric breakdown of the gas.

[2] The pinholes were manufactured by Optimation Hole division, 123 Nashua Rd, suite 172, Londonberry, NH 03053, USA, (603)623-2800

eter D over the transmitted intensity through the Pt foil is $D^2/[D_m^2 \exp(-\mu_{Pt}\rho_{Pt}t)]$, where the density of Pt $\rho_{Pt} = 21.41$ g/cm^3, the Pt thickness $t = 50$ μm, and the mass absorption coefficient of Pt $\mu_{Pt} = 292$ cm^2/g at 7.0 keV. This design was found to work well at 7 keV, since for the smallest pinhole used, $D = 3.5$ μm, this ratio is 1.8×10^9. With approximately 3×10^5 photons/s passing through the pinhole, 1.7×10^{-4} photons/s would be transmitted through the foil! It was found later that this design can be further improved by re-orienting the pinhole with respect to the axis of symmetry[1]. Finally one should note that one can use slits to limit the sample size instead of pinholes[2].

4.6 Demonstration of coherence: Fraunhofer diffraction pattern of a pinhole.

To demonstrate that a hard X-ray beam generated by a second generation synchrotron source is transversally coherent, one would perform a Young's double-slit experiment. Since the transverse coherence length of synchrotron sources at the sample position is only a few μm, we would have to make two pinholes, separated by a few μm, each having a one μm diameter. Since this is difficult to achieve experimentally[3], it is easier to observe the Fraunhofer diffraction pattern of a single pinhole. If the transverse coherence lengths l_x or l_y are too small compared to the pinhole diameter D, then no diffraction pattern would be observed. Otherwise, the Fraunhofer condition

[1] Recently, we found that the axis of maximum transmission through the pinholes was not exactly adjusted with the surface normal of the foils. The pinholes were mounted on a goniometer and centered by rocking the angle of incidence of the incoming radiation. We found that the axis of maximum transmission for the 3.5 μm and 7.5 μm pinholes was tilted by 4.3 and 3° respectively with respect to the axis perpendicular to the mount. An increase in flux of a factor 5 was found for the 3.5 μm pinhole. The pinholes were remounted to fix this problem.

[2] Dr Doug Abernathy has done some recent work on this at ESRF using sharpened Huber slits to observe Fraunhofer diffraction patterns. It seems possible to control these slits accurately and reproducibly.

[3] The first observation of Fraunhofer diffraction patterns with hard X-rays from a rectangular 25 μm wide slit was made by Mancini and Bilderback[85]. Recently, Ferrer et al. [86] observed a Fraunhofer diffraction pattern of an *effective* slit made by an X-ray mirror. In a more recent experiment at ESRF, Comin et al. also observed Young's double-slit interference fringes at the surface diffraction beamline (bl13) of ESRF, using 4.73 KeV X-rays incident on two 0.5cm grazing incidence mirrors separated by 1 cm, which acted like double slits.

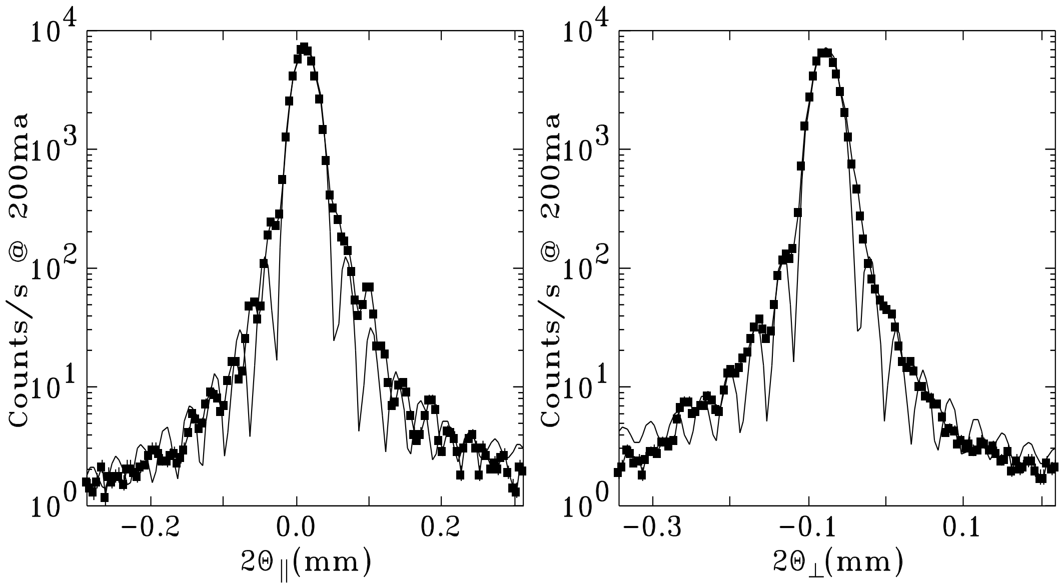

Figure 4.4: Fraunhofer diffraction patterns of a 7.5 μm pinhole resolved with a 8.5 μm pinhole, placed 1.12 m behind the first pinhole. The experiment is performed with 7 keV X-rays, at a ring current of 200 mA. The pinhole was scanned vertically or along $2\Theta_{||}$(Left). A least-squares fit of the Fraunhofer diffraction pattern of a pinhole to Eq. 4.3, with $D = 5.9$ μm is shown with a solid line. (Right) A detector scan in the horizontal, i.e. along $2\Theta_{\perp}$. The fringe contrast is worst along $2\theta_{\perp}$, and the FWHM of the peak is wider than the least-squares fit with $D = 5.9$ μm. As expected, the fringe contrast is better along $2\Theta_{||}$ than along $2\Theta_{\perp}$, because the vertical transverse coherence length is 22 times larger than the horizontal one.

is satisfied and fringes would be observable.

Fig 4.4 shows Fraunhofer diffraction patterns observed at NSLS X-25. This was observed with 1.77 Å X-rays incident on a pinhole with $D = 7.5$ μm, placed 28 m from the source. The X-rays were detected with a scintillator masked by a 8.5 μm pinhole placed 1.12 m from the pinhole. Two scans along $2\Theta_{||}$ and $2\Theta_{\perp}$ are shown. The contrast is excellent, revealing fringes observable over four orders of magnitude.

Recall that the detected intensity of a Fraunhofer diffraction pattern of a circular pinhole, measured by a point detector, is [39]

$$I(r) = \frac{I_0 A^2}{\lambda^2 R_d^2} \frac{4J_1^2(\frac{\pi D r}{\lambda R_d})}{(\frac{\pi D r}{R_d \lambda})^2}, \tag{4.3}$$

where x and y are respectively the horizontal and vertical displacements from the peak center in the detector plane, R_d is the distance between the detector and the pinhole with $r = \sqrt{x^2+y^2} << R_d$, I_0 is the incident intensity on the pinhole and A is the pinhole area. The factor $A^2/(\lambda R_d)^2$ normalizes the integrated intensity to $\int_0^\infty 2\pi r I(r) dr = I_0 A$. This relation assumes a *plane wave illumination* of the pinhole generated by a point source placed far away from the first pinhole. The first zero of this function occurs at $r = 1.22\lambda R_d/D$. Its FWHM is

$$FWHM = \frac{1.0288\lambda R_d}{D}. \tag{4.4}$$

The measured FWHM in Fig 4.4 are respectively 0.0298 mm and 0.0374 mm. Using Eq. 4.4 with $R_d = 1.121$m, one finds $D = 6.9$ and 5.5 μm, which is in good agreement with the 7.5 μm diameter estimated by transmission. A plot of the theoretical Fraunhofer diffraction pattern of a circular pinhole convolved with the detector resolution is shown in both figures. The fit integrates Eq. 4.3 numerically over the detector pinhole area. Six parameters are used: a peak intensity, an input pinhole diameter, a center position, a fixed detector pinhole diameter of 8.5 μm, a constant background, and a linear slope in the background. For the slice along $2\theta_{||}$, the central fifteen data points are well fit, but the calculated fringes are out of phase with the data. For the slice along $2\theta_{\perp}$, the data are broader than the fit, and the fringe contrast is worse than the fringe contrast along $2\theta_{||}$. The phase shift in the fringes and the assymmetric FWHM could be caused by averaging many horizontal coherence lengths in the pinhole diameter, and by spatial fluctuations on the incident intensity profile (see Fig. 4.7). When this occurs, more complicated forms of the theoretical diffraction must be used, like in section 5.7 of Ref. [39] and in Ref. [87].

We also observed these Fraunhofer diffraction patterns with the CCD detector. Using the parallel detection properties of the CCD and its time resolution, one can get more instantaneous properties of the diffracted beam and can test easily for source stability and motion. If the source moves or some upstream optical element moves, it is easy to track with the detector. This is a big advantage of the CCD over the scanning pinhole assembly used in the previous figure. Fig 4.5 shows the time average of the CCD data using an input pinhole diameter $D = 3.5$ μm and a distance pinhole-CCD, $R_d = 1.04$ m using 6.9 keV X-rays. The CCD was exposed for two seconds, and thirty six files were averaged. As seen in the two perpendicular slices in the figure, the central 7×7 pixels are reasonably fit by the Fraunhofer diffraction pattern of a circular pinhole, convolved with the detector's resolution[1] derived in Eq. (3.12). The error bars of the data were calculated using the estimated variance and Eq. (A.14). The fit shown is a non-linear least-squares fit, with a $\chi^2 = 14.4$, $D = 2.57$ μm and a dark count of 0.25 photons/2sec/pixel. This high value of χ^2 is probably caused by several effects, like a non-circular pinhole[2], a finite source size which does not satisfy perfectly the Fraunhofer condition of a point source and an approximate resolution function. This fit has a smaller χ^2 than the fits in Fig 4.4, which were an order of magnitude larger. Since the ratio D/l_x is smaller for the 3.5 μm pinhole, the Fraunhofer diffraction condition is more closely matched with a smaller pinhole. Finally, each scan of the CCD was fit to the model. Fifty one patterns were collected with a cycling time of 10.4 s. The fit centers were constant to a fraction of a pixel size except in one of the scans where the peak center moved by two pixels (45 μrad) in the vertical. This sudden motion was seen in only one of the fifty one scans and seems to be characteristic of the stability at X-25[3]. This angular motion would correspond to a source motion of $2 \times 22.4\mu\text{rad} \times 27.8$ m $= 1.2$ mm which is too large for a vertical source motion. It is most likely caused by some motion of the monochromator, which results in an angular shift.

4.7 Incident X-ray beam structure and stability

Fig. 4.6 shows the time fluctuations of the incident beam at X-25 measured by an ion chamber monitor placed before a 3.5 μm pinhole. The time fluctuations of the total transmitted count rate measured with a scintillation detector placed behind the pinhole are also shown. The relative fluctuations of the detector and monitor signals are respectively 3.5 and 2 %. The detector signal fluctuations are larger than the monitor signal. Furthermore, the fluctuations in the ion chamber monitor signal

[1] The calculated signal is integrated over the area of a pixel. Then it is smeared according to Eq. 3.12.

[2] One can see that the data are not quite circularly symmetric. Furthermore, two stripes are observed in the tails of the diffraction pattern. These stripes are not clearly seen in the previous figure, but they are easily seen far away from the peak.

[3] Prof. Steve Dierker mentioned that their group also observed a similar phenomena at X-25 in their small angle scattering data from gold colloids.

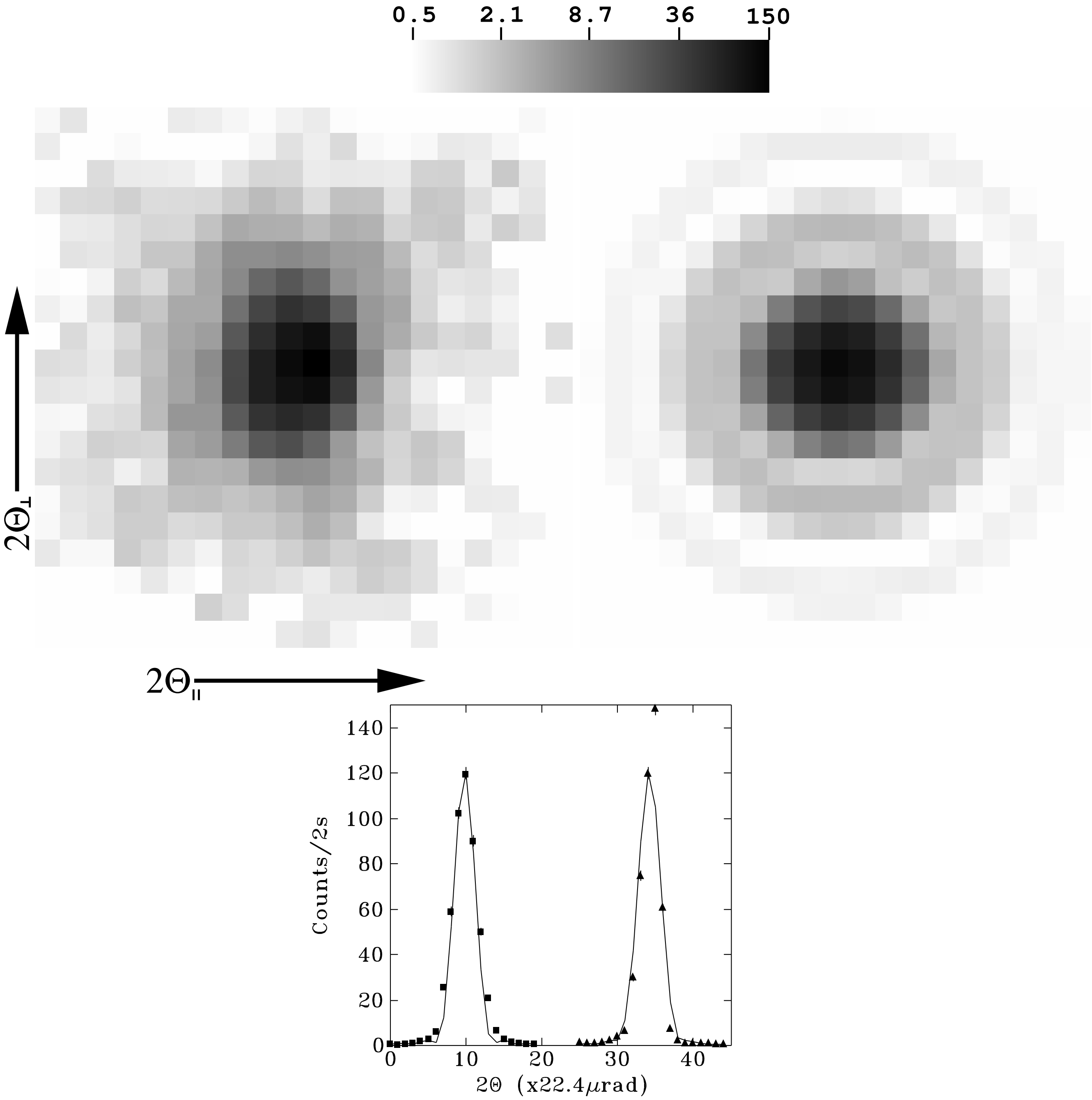

Figure 4.5: A grey scale of the CCD data (top left) for the central 20×20 pixel of the CCD. The grey scale is logarithmic as shown in the legend in photons/2sec/pixel. Each pixel subtends 22.4 μrad. To the right, a least-square fit to a Fraunhofer diffraction pattern of a circular pinhole convolved with the detector resolution discussed in the text. Below, two perpendicular slices of the data (with squares) and fit (solid line).

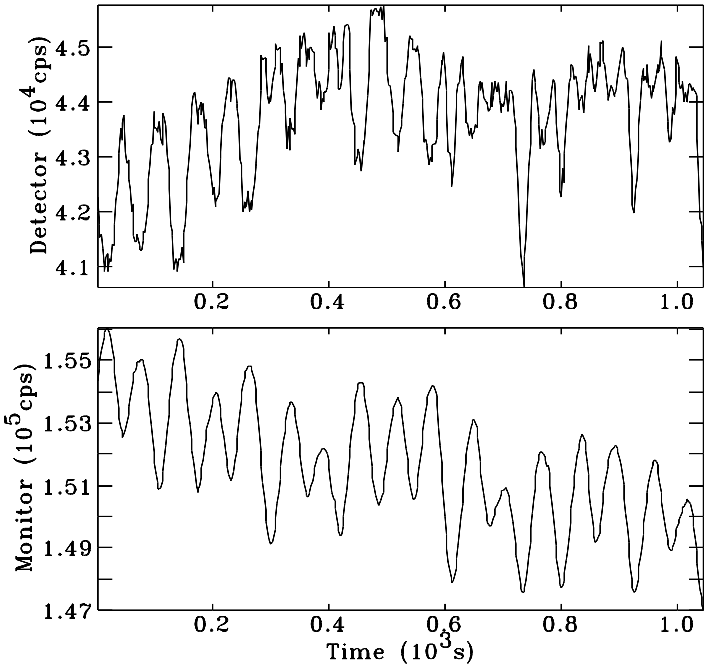

Figure 4.6: (Top) Time fluctuations of the total flux transmitted through a 3.5 μm pinhole. The upstream slits were wide open for this measurement. (Bottom) The ion chamber monitor signal at X-25 before the pinhole. Fluctuations with a period of 62.5 s are present in the incident beam and the transmitted beam.

and the transmitted beam through the pinhole in Fig. 4.6 are anti-correlated. This is very likely a sign of angular fluctuations in the incident beam, modified by the transmission through the pinhole. A Fourier analysis[1] of these fluctuations for the monitor reveals a fundamental period of 62.5 s, with some longer time scales with periods of 100 s. The detector signal shows, in addition to the frequencies found in the monitor signal, faster fluctuations with a period of 31.25 s, which is the second harmonic of the fundamental. These fluctuations appeared also in the beam position monitor signal.

Another group has observed incident intensity fluctuations at X-25 at about 25 Hz. Because, the shortest exposure was 120 s, we integrated over much of these fluctuations, reducing the amplitude of the fluctuations.

Fig. 4.7 shows two scans of the spectrometer table revealing some random structure modulating the incident beam at X-25. These length scales are approximately 20 and

[1]The power spectrum of the signal was calculated numerically. The power spectrum is the square of the Fourier transform.

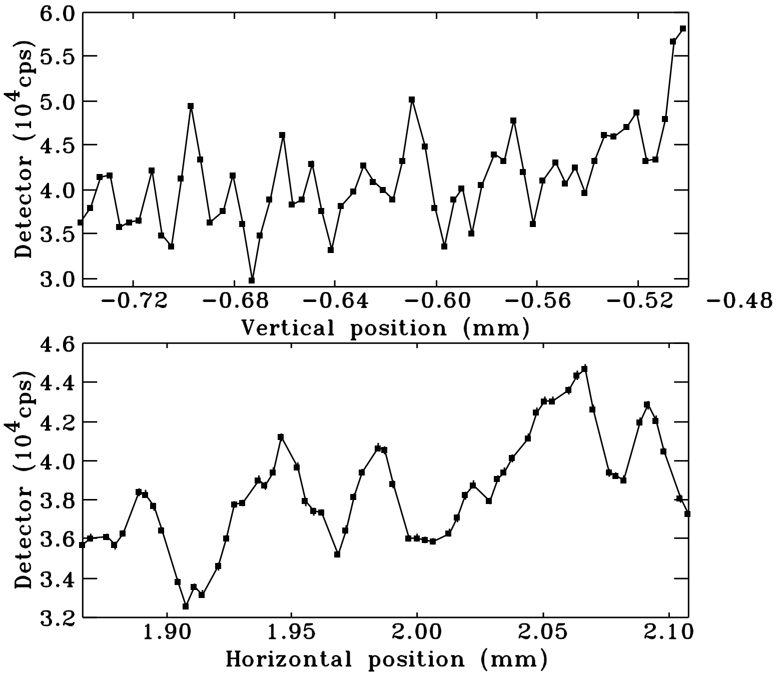

Figure 4.7: The horizontal and vertical structure of the incident beam measured by scanning the spectrometer table perpendicular to the incoming beam direction. The detector was placed behind a 3.5 μm pinhole. Scanning the spectrometer table moves the pinhole along the structure modulating the incident beam. Note that the step size is the same for both plots. This structure is narrowest in the vertical.

40 μm in the vertical and horizontal respectively. This spatial structure is time independent. It is believed that the structure is due to either the monochromator crystal or to some Be window upstream of the pinhole. This structure in the incident beam was observed at CHESS, X25 and ESRF[1]. During the experiment, the incident collimating pinhole was set on a flat region of this structure.

4.8 Temperature calibration and heat treatment

Fig. 4.8 shows a plot of the integrated intensity over an area of 380 $\times$ 190 pixels, as the sample is disordered from below to above T_c. The critical temperature of the order-disorder transition in Cu_3Au is $T_c = 391 \pm 1$ °C. It compares well with the critical temperature of 390°C found in the literature[2]. Before a quench, the

[1] Recently, it was found that the structure in the incident beam at ESRF was due to the small angle scattering from the monochromator Be window. This was observed on a microfocus beamline. They found that the structure observed was imaged from the Be window. By polishing this window, they also showed that the structure disappeared.

[2] See Warren[26], Chapter 12

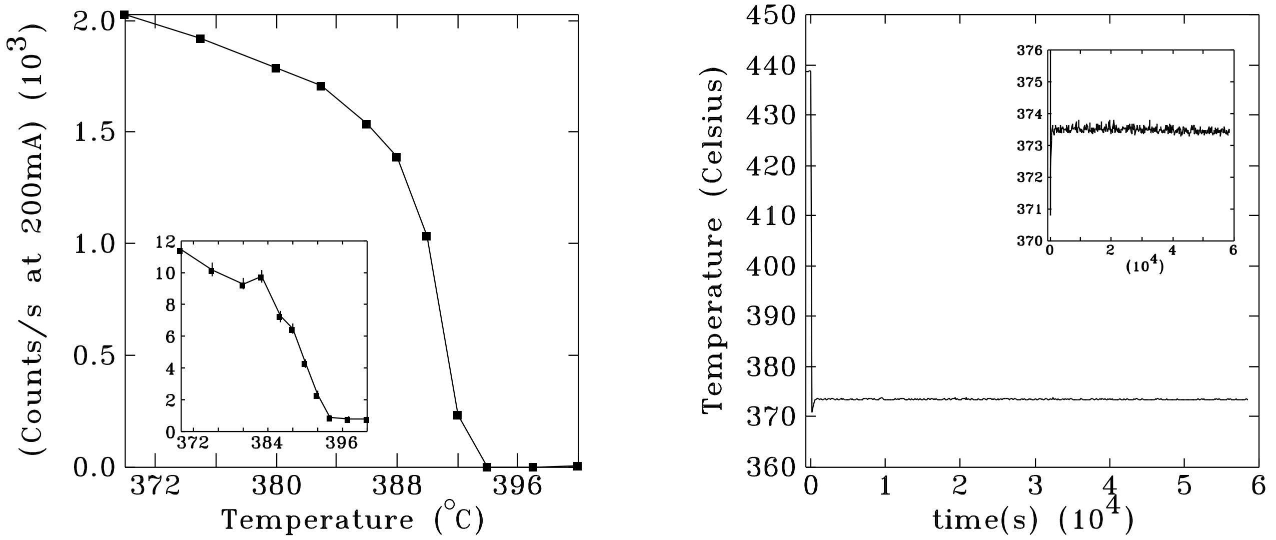

Figure 4.8: Left: Integrated intensity of $S(\vec{q})$ over an area of 380×190 pixels centered on the Cu3Au (100) reflection versus temperature. The inset is the integrated intensity over the parasitic peak discussed in the next section. Its temperature behavior is the same as the (100) peak. Right: The quench profile for Run 21. The temperature read by the second thermocouple is displayed as a function of time after the quench. The sample was annealed near 440 °C and quenched abruptly to its final temperature. The inset shows that after an initial undershoot of 2.5 °C, the temperature is stable to within a fraction of a degree over sixteen hours.

sample was annealed above T_c to remove any long range order. At X25, the sample was annealed at 440°C and then quenched rapidly to its final temperature. Both quenches reported in this thesis for the X25 experiment were made at the same final set point temperature $T = 370$ °C, or $t = T_c - T = 21$ °C. The temperature after an initial undershoot of approximately 2.5 °C was constant within ± 0.5 °C for 20 hours (See a typical quench profile in Fig. 4.8).

At CHESS, the sample was annealed slightly above T_c and quenched to a final temperature of $t = 22$ °C. After an initial undershoot of 3 °C, the second thermometer drifted up by 5 °C during the 10 hour experiment although the setpoint temperature stayed constant. If this temperature drift is characteristic of the illuminated area, this could affect the kinetics of the ordering process.

4.9 Setting the angle of incidence θ_i

Below T_c, for θ set at the Bragg condition, the structure factor consisted of a narrow peak superimposed on a broad order-disorder peak of Cu_3Au (100). The narrow component would move across the detector plane by scanning the angle of incidence on the sample. Changing θ_i by an angle Δ moved this peak in 2θ by 2Δ. The integrated intensity in this peak was maximized when θ was set to the Bragg angle, while the broad order-disorder peak became weaker at the Bragg condition. A radial θ-2θ scan along the (100) had a FWHM of $\Delta\theta = 0.1$ °. Furthermore, this peak disappeared above T_c, which implies that it must be related to the order-disorder phase transition in Cu_3Au, and not to something like an oxide peak. Using $dq/q = tan^{-1}(\theta)\Delta\theta$, with $\theta = 14.54°$, one finds that this scattering could be caused by a surface layer approximately 500 Å thick. In the experiments reported next, the Bragg angle was offset by 0.1 °, in order to look only at scattering from the bulk sample. Some fraction of the signal on the (100) is lost because of this offset.